Available online at www.sciencedirect.com
ScienceDirect
Journal of Computational Physics 226 (2007) 1859–1873
JOURNAL OF COMPUTATIONAL PHYSICS
www.elsevier.com/locate/jcp

Consistent inflow and outflow boundary conditions for transported probability density function methods

D.W. Meyer *, P. Jenny

Institute of Fluid Dynamics, Sonneggstrasse 3, ETH Zurich, Switzerland

Received 16 October 2006; received in revised form 9 May 2007; accepted 12 June 2007
Available online 22 June 2007

Abstract

In transported probability density function (PDF) methods, the PDF transport equations are most often solved with realization based techniques using particles. In this paper, a consistent treatment of particle in- and outflow boundary conditions for transported PDF methods is devised. It is shown that the presented approach is simple and, most important, consistent with the underlying Eulerian PDF transport equation. This is not the case for other boundary condition implementations discussed in the literature, especially if the fluctuating particle velocities are high compared with the averaged ones.
© 2007 Elsevier Inc. All rights reserved.

MSC: 65C35; 65C20

PACS: 02.70.Uu; 47.27.Jv; 47.70.Fw

Keywords: PDF method; Boundary condition; Particle method

1. Introduction

Although the dynamics of turbulent flows can exactly be described by the Navier–Stokes equations, slight variations of the boundary or initial conditions are amplified by turbulence, leading to different flow fields. Therefore, flow properties can be considered as random variables. Perhaps the most rigorous approach in that sense are transported probability density function (PDF) methods. Aside from their strong adoption of the randomness concept, PDF methods have properties, which make them very attractive for the application to turbulent flows [1]. In contrast to other approaches such as Reynolds averaged Navier–Stokes or large-eddy simulation, all convective transport terms are closed. Moreover, important for turbulent reactive flow simulations [2], the highly non-linear reaction source term appears in closed form, which leads to less assumptions and uncertainties. In most PDF methods for turbulent combustion, only single point PDF's are considered.

* Corresponding author. Tel.: +41 44 632 26 54; fax: +41 44 632 11 47.
E-mail address: meyer@ifd.mavt.ethz.ch (D.W. Meyer).

0021-9991/$ - see front matter © 2007 Elsevier Inc. All rights reserved.
doi:10.1016/j.jcp.2007.06.014

Therefore, conditional averages of spatial derivatives need to be modeled. For example, molecular diffusion in the joint velocity–composition or the joint composition PDF transport equation has to be closed by a mixing model [3]. However, in the PDF modeling framework, such closure problems can be addressed from an Eulerian or a Lagrangian viewpoint. The PDF transport equation is formulated in an Eulerian reference system [4,5], but is solved with Lagrangian methods using particles whose evolution is described by stochastic differential equations (SDE). A relation between the SDE's and the Eulerian PDF transport equation is given through the Lagrangian PDF transport equation, which is equivalent to the SDE's [6]. Mass conservation, which plays a role in connecting the Lagrangian and the Eulerian PDF transport equations, leads to a condition for the marginal particle position PDF. Implications of this condition for the Eulerian PDF transport equation are discussed in [7]. Apart from the particle transport scheme, which is relevant inside the computational domain, the consistency condition should be honored by appropriate in- and outflow boundary conditions. Unfortunately, whether in the contributions by Pope and co-workers [8–11] nor in the publications by Lindstedt and co-workers [12,13], the authors could find any details about the particle treatment at boundaries in joint velocity–composition PDF algorithms. In Welton and Pope [14], however, where a joint velocity PDF method is combined with smooth particle hydrodynamics, the use of particle buffer layers at in- and outflow boundaries is described. For joint composition PDF methods, Fox presents in Chapter 7.3.3 of [5] an implementation of in- and outflow boundary conditions. Other work summarized by Gardiner [15] or the more specific paper by Valiño and Hierro [16] provide a theoretical perspective on boundary conditions in PDF methods; details about the implementation involving particles, however, are not provided. Even though such implementations are hardly discussed in the literature, the subject is not trivial: for example, it will be shown that in general the approaches by Welton and Pope, and Fox do not honor the consistency condition mentioned above and may lead to inaccurate results in the vicinity of in- or outflow boundaries. Mass conservation correction algorithms, as developed by Rembold and Jenny [17], Zhang and Haworth [18] or Muradoglu et al. [19], may hide mass conservation inconsistencies. In this paper, a consistent approach will be presented, where moving, reflecting walls are used at in- and outflow boundaries. A slightly different concept was applied by Werder et al. [20] for molecular dynamics simulations.

The paper is organized as follows. In Section 2, the link between the Eulerian and Lagrangian PDF transport equations is outlined and the previously mentioned consistency condition is highlighted. To keep the notation in this section as simple as possible, we focus mainly on constant density flows. In Section 3, an implementation of in- and outflow boundary conditions, which fulfills the consistency condition, is devised and compared with the ones outlined by Welton and Pope [14], and Fox [5]. Numerical investigations, focusing on boundary condition effects, are presented in Section 4 and concluding remarks are made in Section 5.

2. Consistency with mass conservation

Based on the momentum and composition conservation equations, a transport equation for the joint velocity–composition PDF $f(\mathbf{V},\boldsymbol{\psi};\mathbf{x},t)$ can be derived [6 (Appendix H),4 (Section 3.5),5 (Chapter 6.2)]. Here, $\mathbf{V}$ is the sample space vector of the velocity field $\mathbf{U}(\mathbf{x},t)$, $\boldsymbol{\psi}$ the sample space vector of the composition field $\boldsymbol{\phi}(\mathbf{x},t)$, $\mathbf{x}$ the position in physical space and t is the time. $f(\mathbf{V},\boldsymbol{\psi};\mathbf{x},t)$ is called an Eulerian PDF, since it is given at specific positions $\mathbf{x}$. Since $f(\mathbf{V},\boldsymbol{\psi};\mathbf{x},t)$ depends on a large number of variables, standard techniques (e.g., finite-volume methods) are inappropriate. Most often, particles are used to solve such PDF transport equations. Therefore, a Lagrangian viewpoint is adopted, where $\mathbf{X}^+(t,\mathbf{X}_0^+)$ denotes the position of a fluid particle at time t that originates from $\mathbf{X}_0^+$ at time t_0. The fluid particle velocity $\mathbf{U}^+(t,\mathbf{X}_0^+)=\mathbf{U}(\mathbf{X}^+(t,\mathbf{X}_0^+),t)$ is equal to the derivative of $\mathbf{X}^+$ in time. The corresponding Lagrangian probability density function $f_L(\mathbf{V},\boldsymbol{\psi},\mathbf{x};t|\mathbf{x}_0)$ is the fluid particle joint velocity–composition–position PDF. Here, $\mathbf{V}$, $\boldsymbol{\psi}$, $\mathbf{x}$ and $\mathbf{x}_0$ are the sample space variables of $\mathbf{U}^+$, $\boldsymbol{\phi}^+$, $\mathbf{X}^+$ and $\mathbf{X}_0^+$, respectively. Based on so-called fine-grained PDF's and mass conservation, Pope derived the relation

$$\int f_L(\mathbf{V},\boldsymbol{\psi},\mathbf{x};t|\mathbf{x}_0)\,\mathrm{d}\mathbf{x}_0 = f(\mathbf{V},\boldsymbol{\psi};\mathbf{x},t) \tag{1}$$

(Eq. (12.80) in [6]), which connects the Eulerian with the Lagrangian PDF. There and from now on, the integral operator indicates integration over the whole corresponding space. Moreover, mass conservation leads to

a consistency condition for the position PDF $f(\mathbf{x};t|\mathbf{x}_0)$: integration of the fine-grained position PDF $f'(\mathbf{x};t|\mathbf{x}_0) = \delta(\mathbf{X}^+(t,\mathbf{x}_0) - \mathbf{x})$, expressed as a δ-function, leads to

$$\int f'(\mathbf{x};t|\mathbf{x}_0)\,\mathrm{d}\mathbf{x}_0 = \int \delta(\mathbf{X}^+(t,\mathbf{x}_0) - \mathbf{x})\,\mathrm{d}\mathbf{x}_0 = \int \delta(\mathbf{X}^+(t,\mathbf{x}_0) - \mathbf{x})\,\mathrm{d}\mathbf{X}^+ = 1. \tag{2}$$

The second integral could be replaced by an integral over the particle positions $\mathbf{X}^+$, since $\mathrm{d}\mathbf{x}_0[(\partial\mathbf{X}^+)/(\partial\mathbf{x}_0)] = \mathrm{d}\mathbf{X}^+$ (Eq. (2.29) in [6]). Here, the factor connecting $\mathrm{d}\mathbf{x}_0$ and $\mathrm{d}\mathbf{X}^+$ is the determinant of the Jacobian, which is unity for constant density flows. With Eq. (2) and the well-known relation $f(\mathbf{x};t|\mathbf{x}_0) = \langle f'(\mathbf{x};t|\mathbf{x}_0)\rangle$ between PDF and fine-grained PDF (similar to Eq. (H.4) in [6]), one obtains

$$\int f(\mathbf{x};t|\mathbf{x}_0)\,\mathrm{d}\mathbf{x}_0 = 1. \tag{3}$$

Rewriting this integral using Bayes theorem and setting $f(\mathbf{x};t_0) = f(\mathbf{x}_0) = 1/\mathcal{V}$, which corresponds to a uniform initial particle position PDF, leads to

$$\int f(\mathbf{x};t|\mathbf{x}_0)\,\mathrm{d}\mathbf{x}_0 = \int \frac{f(\mathbf{x},\mathbf{x}_0;t)}{f(\mathbf{x}_0)}\,\mathrm{d}\mathbf{x}_0 = \mathcal{V}\int f(\mathbf{x},\mathbf{x}_0;t)\,\mathrm{d}\mathbf{x}_0 = \mathcal{V}f(\mathbf{x};t), \tag{4}$$

where $\mathcal{V}$ is the volume of the flow domain considered. Combining Eqs. (3) and (4) results in

$$f(\mathbf{x};t) = 1/\mathcal{V} \tag{5}$$

and therefore, mass conservation used for the derivation of Eq. (1) implies that a uniform particle position PDF remains uniform in time. Note that this consistency condition holds whether joint velocity–composition or joint composition PDF methods are considered. A corresponding condition for low Mach number compressible flows is given by Eq. (3.82) of [4], relating the position PDF to the average mass density. In Chapter 6.7.3 of [5], Fox developed condition (5) using the Lagrangian PDF transport equation: multiplying it with $f(\mathbf{x}_0)$ and integrating over the whole $\mathbf{x}_0$–$\mathbf{V}$-space results in

$$\frac{\partial f(\mathbf{x};t)}{\partial t} + \frac{\partial}{\partial x_i}[\langle U_i|\mathbf{x}\rangle f(\mathbf{x};t)] = 0. \tag{6}$$

This can be obtained from Eq. (4.31) in [4] as well for low Mach number compressible flow. Therefore, if $f(\mathbf{x};t_0) = 1/\mathcal{V}$ and if the divergence of the conditional expectation $\langle U_i|\mathbf{x}\rangle$ is zero, $f(\mathbf{x};t)$ remains constant for $t > t_0$. A different, third derivation of condition (5) is given in Chapter 12.6.2 of [6].

After having highlighted the connection between mass conservation and the particle distribution, we turn now to the motion of particles in sample space. Analogous to the connection between the Fokker–Planck and the Langevin equation [15], the stochastic differential equations (SDE)

$$\mathrm{d}X_i^* = U_i^*\,\mathrm{d}t = (\langle U_i|\mathbf{X}^*\rangle + u_i^*)\,\mathrm{d}t \tag{7}$$

and

$$\mathrm{d}U_i^* = -\frac{1}{\rho}\left(\frac{\partial\langle p\rangle}{\partial x_i}\right)_{\mathbf{X}^*}\mathrm{d}t - \left(\frac{1}{2}+\frac{3}{4}C_0\right)\frac{\varepsilon(\mathbf{X}^*)}{k(\mathbf{X}^*)}(U_i^* - \langle U_i|\mathbf{X}^*\rangle)\,\mathrm{d}t + \sqrt{C_0\varepsilon(\mathbf{X}^*)}\,\mathrm{d}W_i(t) \tag{8}$$

result from the Lagrangian PDF transport equation. Note that in the first equation the Reynolds decomposition was used and the second equation includes the simplified Langevin model (SLM) as a possible closure of the PDF transport equation [21]. There, p is the pressure, C_0 a model constant, ε the dissipation rate of the turbulent kinetic energy k and $\mathrm{d}W_i(t)$ a Wiener process. The superscript * is used to point out that we no longer deal with fluid but now with model particles.[1] Eqs. (7) and (8) are evolution equations typically solved in joint velocity PDF methods for an ensemble of particles.

If the Lagrangian PDF transport equation is averaged over velocity sample space, one obtains the SDE

$$\mathrm{d}X_i^* = \langle U_i|\boldsymbol{\phi}^*,\mathbf{X}^*\rangle\,\mathrm{d}t = (\langle U_i|\mathbf{X}^*\rangle + \langle u_i|\boldsymbol{\phi}^*,\mathbf{X}^*\rangle)\,\mathrm{d}t \tag{9}$$

[1] Often also called stochastic or notional particles.

in the context of transported joint composition PDF methods. Like in Eq. (7), a deterministic and a random term are present. A model for the unclosed random term in Eq. (9), involving a Wiener process, is presented in Eq. (7.27) of [5].

Now, a large number of model particles can be transported numerically according to Eqs. (7) and (8), or (9). The model particles are uniformly distributed in physical space at initial time t_0 and in order to honor condition (5) they have to remain uniformly distributed for $t > t_0$. From the ensemble of model particles, statistical quantities such as $\langle \boldsymbol{\phi}|\mathbf{x}\rangle$ or $\langle \phi_\alpha u_i|\mathbf{x}\rangle$[2] can be estimated for each position $\mathbf{x}$ and time t. More information about estimating statistical moments is given in Chapter 12.6.3 of [6], Chapters 7.3.4 and 7.4.4 of [5], or Section 6.7 of [4]. For compressible flows, instead of a PDF transport equation, a similar equation for the mass density function (MDF) $\mathcal{F}(\mathbf{V},\boldsymbol{\psi};\mathbf{x},t) \equiv \rho(\boldsymbol{\psi})f(\mathbf{V},\boldsymbol{\psi};\mathbf{x},t)$ is solved [4]. Moreover, in addition to velocity, composition and position, each particle represents a mass Δm. After highlighting the role of the position PDF $f(\mathbf{x};t)$, we now turn to the consistent implementation of particle in- and outflow boundary conditions.

3. Particle in- and outflow boundary conditions

Although mainly constant density flow was considered in the previous section, the following considerations are also valid for variable density. The purpose of particle in- and outflow boundary conditions is to supply or remove particles at open domain boundaries. This should be performed at rates, which are consistent with condition (5) or Eq. (3.82) of [4] for low Mach number compressible flows. Otherwise, mass conservation is violated leading to errors in the particle position PDF $f(\mathbf{x};t)$ as shown in Section 2 (Eq. (6)). For illustration purposes, a one-dimensional, time independent configuration with $f(V;x,t) = f(V;x)$ is considered.

3.1. Outflow boundary condition

At an outflow boundary ($x = x_\mathrm{b}$), the mean velocity $\langle U|x_\mathrm{b}\rangle$ points out of the flow domain. It can be determined by

$$\langle U|x_\mathrm{b}\rangle = \int_{-\infty}^{\infty} Vf(V;x_\mathrm{b})\,\mathrm{d}V = \int_{-\infty}^{0} Vf(V;x_\mathrm{b})\,\mathrm{d}V + \int_{0}^{\infty} Vf(V;x_\mathrm{b})\,\mathrm{d}V, \tag{10}$$

or in a particle method by sampling all model particles that cross the boundary. Here, $f(V;x_\mathrm{b})$ is the Eulerian velocity PDF and in the second step, the integration was decomposed into the contributions by in- and outflowing particles represented by the first and second terms, respectively (for $\langle U|x_\mathrm{b}\rangle > 0$). In Chapter 7.3.3 of [5], Fox mentions that the out going particles can simply be eliminated. In Eq. (10), this would correspond to eliminating the first integral. Since this integral is negative ($V \in (-\infty, 0]$), the resulting mean velocity becomes too high. Moreover, this leads to a loss of mass in the vicinity of the boundary and to incorrect statistics, e.g., $\langle uu|x_\mathrm{b}\rangle$. Although the error remains small if $\langle U|x_\mathrm{b}\rangle$ is much larger than the root mean square (rms) velocity u' of U^*, it becomes prominent for small values of $\langle U|x_\mathrm{b}\rangle$. Therefore, we refer to this approach as 'convection dominated outflow boundary condition'.

For $\langle U|x_\mathrm{b}\rangle \to 0$, the outflow boundary can be replaced by a symmetry or slip-wall boundary, which can be implemented by reflecting the particles at the boundary. In that case, Eq. (10) can be written as

$$\langle U|x_\mathrm{b}\rangle = \int_{0}^{\infty} (-V)f(V;x_\mathrm{b})\,\mathrm{d}V + \int_{0}^{\infty} Vf(V;x_\mathrm{b})\,\mathrm{d}V = 0. \tag{11}$$

The frequency interpretation of Eq. (11) for N particles crossing the boundary from inside the domain is

$$\langle U|x_\mathrm{b}\rangle_{2N} = \frac{1}{2N}\left(\sum_{n=1}^{N}(-U^{*(n)}) + \sum_{n=1}^{N} U^{*(n)}\right) = 0, \tag{12}$$

where the first and second sums correspond to the reflected (inflowing) and outflowing particles, respectively. For $\langle U|x_\mathrm{b}\rangle > 0$, an appropriate outflow boundary implementation, which is not restricted to high $\langle U|x_\mathrm{b}\rangle$, is

[2] Note that $\langle \boldsymbol{\phi}|\mathbf{x}\rangle = \langle \boldsymbol{\phi}\rangle(\mathbf{x})$ and $\langle \phi_\alpha u_i|\mathbf{x}\rangle = \langle \phi_\alpha u_i\rangle(\mathbf{x})$.

based on a reflecting wall moving with the velocity $\langle U|x_b\rangle$. Note that in the moving reference frame, the velocity of particle n is $W^{*(n)} = U^{*(n)} - \langle U|x_b\rangle$. Replacing $U^{*(n)}$ in Eq. (12) by $W^{*(n)}$ and adding $\langle U|x_b\rangle$ leads to the corresponding equation for the moving, reflecting wall in the stationary reference frame

$$\begin{aligned}\langle U|x_b\rangle &= \frac{1}{2N}\left(\sum_{n=1}^{N}(-W^{*(n)}) + 2N\langle U|x_b\rangle + \sum_{n=1}^{N} W^{*(n)}\right)\\ &= \frac{1}{2N}\left(\sum_{n=1}^{N}(-U^{*(n)} + 2\langle U|x_b\rangle) + \sum_{n=1}^{N} U^{*(n)}\right).\end{aligned} \tag{13}$$

In the second step $U^{*(n)} - \langle U|x_b\rangle$ was substituted for $W^{*(n)}$. The first sum on the second line of Eq. (13) represents the reflected particles. If this moving wall is located at $x = x_0 = x_b - \langle U|x_b\rangle\Delta t$ at $t = t_0$ it will be at $x = x_b$ after the time interval Δt. To make sure that the velocity of the moving wall is consistent with the mean flow velocity, we require that $\langle U|x\rangle = \langle U|x_b\rangle$ in the interval $x \in [x_0, x_b]$. Higher order methods, where $\langle U|x\rangle$ is varying within $[x_0, x_b]$, are conceivable. More details for a linearly varying mean velocity are given in the Appendix. A particle trajectory in the vicinity of such a moving-wall outflow boundary is sketched in Fig. 1. This outflow boundary concept results in an average particle flow with velocity $\langle U|x_b\rangle$ across the boundary honoring the consistency condition discussed in Section 2. The influence on $\langle U|x_b\rangle$ by the particles behind the moving wall (at $x > x_0$ for $t = t_0$) is represented in Eq. (13) by the reflected particles in front of the wall (at $x < x_0$ for $t = t_0$). Therefore, the particles behind the wall can be eliminated at t_0. The particles that moved out of the domain during the time interval Δt are reflected back into the domain according to

$$\begin{aligned}X^{*(n)} &\to x_b - (X^{*(n)} - x_b),\\ U^{*(n)} &\to \langle U|x_b\rangle - (U^{*(n)} - \langle U|x_b\rangle).\end{aligned} \tag{14}$$

Although the previous derivations were made for $\langle U|x_b\rangle > 0$, the mapping (14) also applies for outflow boundaries with $\langle U|x_b\rangle < 0$. Moreover, the presented approach can be employed for time dependent problems, provided the time step Δt is small enough.

3.2. Inflow boundary condition

3.2.1. Moving-wall inflow boundary condition

Analogously, the concept outlined in the previous section is applicable for inflow boundary conditions. Here, the mean velocity $\langle U|x_b\rangle$ is specified at the inflow boundary ($x = x_b$) and is pointing into the flow domain as sketched in Fig. 2 for $\langle U|x_b\rangle > 0$. Other than at outflow boundaries, new particles have to be supplied at $t = t_0$ within the interval $[x_0, x_b]$. Hereby, it is important that the particle density is consistent with the one specified at the inflow. Moreover, the statistics of other particle properties (e.g., of U^* and ϕ^*) have to be in agreement with the specified joint PDF. As sketched in Fig. 2, particles crossing the moving wall during the time interval Δt are reflected back into the flow domain according to the same mapping (14) as for the outflow boundaries.

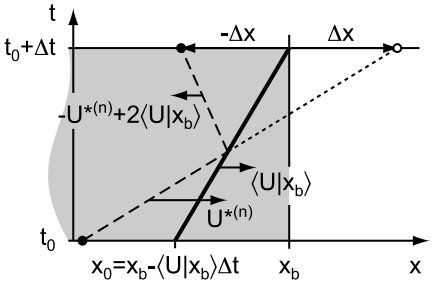

Fig. 1. Particle reflection at moving-wall outflow boundary. The shaded area represents the flow domain and the thick line the moving wall.

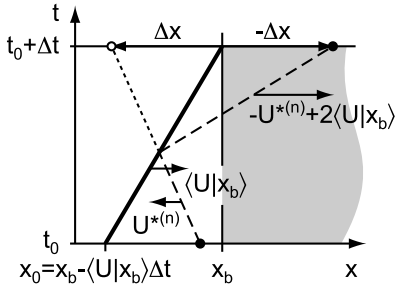

Fig. 2. Particle reflection at moving-wall inflow boundary. The shaded area represents the flow domain and the thick line the moving wall.

3.2.2. Convection dominated inflow boundary condition

In Chapter 7.3.3 of [5], Fox describes a different inflow boundary condition implementation for joint composition PDF methods: during the time interval Δt, M new particles with indices $n \in [1, M]$ are fed into the domain, where M is chosen such that mass conservation is fulfilled. As in the case of slip-wall boundary conditions, the N particles with indices $n \in [M+1, M+N]$ that would have scattered outside the domain, are reflected back into the domain. If we apply this formulation in the joint velocity–composition or joint velocity PDF context, the mean velocity at the boundary becomes

$$\frac{1}{2N+M}\left(\sum_{n=1}^{M} U^{*(n)} + \sum_{n=M+1}^{M+N} U^{*(n)} + \sum_{n=M+1}^{M+N} (-U^{*(n)})\right) = \frac{M}{2N+M}\langle U|x_\mathrm{b}\rangle_M. \tag{15}$$

Note that the correct mean velocity $\langle U|x_\mathrm{b}\rangle$ is honored only if M or N are zero, which corresponds to $\langle U\rangle/u' = 0$ or $u'/\langle U\rangle = 0$, respectively.

In joint composition PDF methods, the particles are transported as given by Eq. (9) or in a more compact form $\mathrm{d}X^* = (\langle U|X^*\rangle + u^*_\phi)\,\mathrm{d}t$, where $\langle u^*_\phi\rangle \equiv 0$. Here, no particle boundary condition for the velocity is required. Therefore, we have similarly to Eq. (15) for the average velocity at the boundary

$$\frac{1}{2N+M}\left(\sum_{n=1}^{M}\left(\langle U|x_\mathrm{b}\rangle + u^{*(n)}_\phi\right) + \sum_{n=M+1}^{M+N}\left(\langle U|x_\mathrm{b}\rangle + u^{*(n)}_\phi\right) + \sum_{n=M+1}^{M+N}\left(\langle U|x_\mathrm{b}\rangle - u^{*(n)}_\phi\right)\right) \approx \langle U|x_\mathrm{b}\rangle. \tag{16}$$

This is equivalent to what we obtain from the moving-wall boundary in the joint composition PDF context.

3.2.3. Reassigning particle velocities

Regarding mass conservation, the inflow boundary implementation presented in Section 3.2.1 is consistent. However, in joint velocity–composition PDF methods, where the marginal velocity PDF $f(V;x,t)$ shows spatial variation in the vicinity of the boundary, it may be necessary to enforce the prescribed PDF there. This can be achieved by reassigning velocities to the reflected particles such that the statistics are consistent with $f(V;x_\mathrm{b},t)$. Note: like at an outflow boundary, the reflected particles represent the particles, which were located behind the moving wall. With a spatially independent density and velocity PDF at $x < x_\mathrm{b}$, the probability that a particle with position $x < x_0$ at time t_0 crosses the moving wall during the time interval Δt with the velocity V is

$$f_\mathrm{b}(V|x) = \begin{cases} \beta f(V;x_\mathrm{b}) & \text{if } [(V - \langle U|x_\mathrm{b}\rangle)\Delta t > x_0 - x \wedge x < x_0], \\ 0 & \text{else,} \end{cases} \tag{17}$$

where β is a normalization constant. Note that the condition $[(V - \langle U|x_\mathrm{b}\rangle)\Delta t > x_0 - x \wedge x < x_0]$ implies $V > \langle U|x_\mathrm{b}\rangle$. Then, using Bayes theorem, the velocity PDF of particles that cross the boundary within Δt and starting from any $x < x_0$ is given by

$$f_\mathrm{b}(V) = \begin{cases} \int_{-\infty}^{x_0} f_\mathrm{b}(V|x) f(x)\,\mathrm{d}x & \text{if } V > \langle U|x_\mathrm{b}\rangle, \\ 0 & \text{else.} \end{cases} \tag{18}$$

Since for $x < x_0$ and constant density, $f(x)$ is uniform (condition (5)), the integral can be simplified as

$$\int_{-\infty}^{x_0} f_b(V|x) f(x)\,dx \propto \int_{-\infty}^{x_0} f_b(V|x)\,dx \propto \int_{x_0 - v\Delta t}^{x_0} f(V;x_b)\,dx \propto v f(V;x_b), \tag{19}$$

where in the second step the substitution $v = V - \langle U|x_b\rangle$ was used. With the normalization condition for PDF's, i.e.,

$$\int_{-\infty}^{\infty} f_b(V)\,dV = 1, \tag{20}$$

the PDF $f_b(V)$ of the reflected particle velocities is fully determined. For a Gaussian PDF $f(V;x_b)$ with standard deviation u' we finally obtain

$$f_b(v + \langle U|x_b\rangle) = \begin{cases} \frac{v}{(u')^2} \exp\left(-\frac{v^2}{2(u')^2}\right) & \text{if } v > 0, \\ 0 & \text{else.} \end{cases} \tag{21}$$

Due to the discrete particle distribution and the wall motion, this is not a Gaussian PDF: for $\langle U|x_b\rangle = 1$ and $u' = 0.5$, the PDF $f_b(V)$ is plotted in Fig. 3. The cumulative distribution function (CDF) of the PDF (21) is

$$F_b(v + \langle U|x_b\rangle) = \begin{cases} 1 - \exp\left(-\frac{v^2}{2(u')^2}\right) & \text{if } v > 0, \\ 0 & \text{else.} \end{cases} \tag{22}$$

This CDF can be inverted and consequently samples with a consistent PDF generated by

$$U_r^{*(n)} = \sqrt{2}u'\sqrt{-\ln(1-\xi)} + \langle U|x_b\rangle, \tag{23}$$

where $\xi \in [0,1]$ is a uniformly distributed random number. The mapping, as for the pure reflection (14), is then

$$\begin{aligned} X^{*(n)} &\to x_b - \frac{U_r^{*(n)} - \langle U|x_b\rangle}{\langle U|x_b\rangle - U^{*(n)}}\left(X^{*(n)} - x_b\right), \\ U^{*(n)} &\to U_r^{*(n)}. \end{aligned} \tag{24}$$

First, the particle position is updated (upper line) and second, the velocity is reassigned (lower line). The expressions (23) and (24) are given for a positive inflow velocity $\langle U|x_b\rangle$.

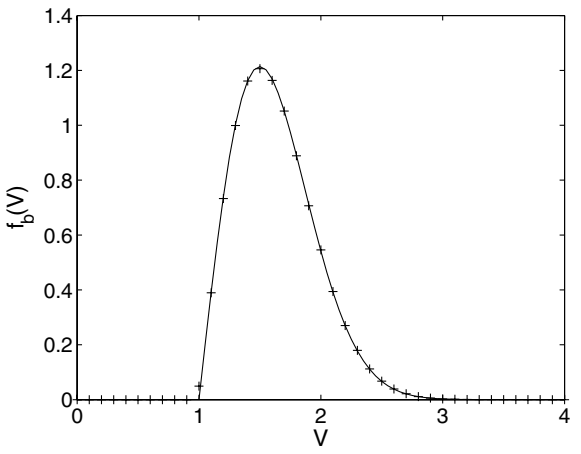

Fig. 3. PDF of the reflected particle velocity $f_b(V)$ for $\langle U|x_b\rangle = 1$ m/s and $u' = 0.5$ m/s. Line: Eq. (21); symbols: histogram of numerical experiment with approximately one million samples.

3.3. Particle buffer-layer boundary conditions

Another straightforward approach for the treatment of particles at boundaries is to use particle buffer-layers as outlined in [14]. In connection with smooth particle hydrodynamics, this approach has the advantage that statistics can be estimated near the boundaries in the same way as inside the domain. However, similar problems as for the convection dominated outflow boundary condition occur at both in- and outflow. No matter how small the time step or how large the size of the layer is chosen, there is always a tendency that high velocity particles, which scattered out of the domain, cannot be fully compensated by incoming particles, because the buffer-layer has only a limited thickness.

4. Numerical validation

In the previous section, it was demonstrated that the consistent treatment of the boundary-surface-normal position and velocity components is essential for mass conservation. Therefore, one-dimensional configurations with variable turbulence intensity $u'/\langle U\rangle$ are ideal to reveal weaknesses of the different boundary condition implementations. In the first test case, convected stationary homogeneous turbulence (CSHT) is simulated. Here, by varying the mean flow velocity, the influence of the turbulence intensity at the boundaries can be investigated. The second case is similar to decaying grid turbulence (DGT), involving turbulence intensity gradients at in- and outflow boundaries. At the inflow, however, much higher turbulence intensities were used, compared to wind-tunnel experiments [22]. Even though the selected test cases are physically very simple, they reveal flaws of the boundary condition implementations very transparently with almost no other interfering effects.

The buffer-layer boundaries are not validated here, since the performance depends, as mentioned in Section 3.3, strongly on the time-step size and layer thickness, and therefore results cannot be fully conclusive.

4.1. Numerical methods

A one-dimensional joint velocity–frequency PDF solution algorithm was implemented for the simulation of incompressible DGT. This is one of the simplest and most fundamental turbulent flows, which has been studied extensively in wind-tunnel experiments [22]. Typically, turbulence is generated by a grid. In a frame of reference moving with the mean flow velocity, the turbulence can approximately be regarded as decaying homogeneous turbulence (sufficiently far away from the grid). Only in the mean flow direction variations of statistical moments have to be considered. We choose the coordinate system such that $\langle U_1\rangle = \langle U\rangle$ is the only non-zero mean velocity component, which is constant in time and space (for incompressible, one-dimensional flow). Moreover, we assume that the velocity statistics are isotropic and Gaussian at the inflow boundary. With these assumptions, the particle evolution Eqs. (7) and (8) can be simplified to

$$\mathrm{d}X^* = (\langle U\rangle + u^*)\,\mathrm{d}t \tag{25}$$

and

$$\mathrm{d}u^* = -\left(\frac{1}{2}+\frac{3}{4}C_0\right)\frac{\varepsilon(X^*)}{k(X^*)}u^*\,\mathrm{d}t + \sqrt{C_0\varepsilon(X^*)}\,\mathrm{d}W(t), \tag{26}$$

respectively. Here, the mean pressure gradient was neglected. For example, on p. 57 of [23], Anand and Pope argue that the mean pressure gradient term in the Eulerian PDF transport equation is small for decaying grid turbulence and can be neglected. The turbulent kinetic energy $k(x) = \frac{3}{2}\langle u^2|x\rangle$ can be evaluated from the particle statistics, but the dissipation rate ε requires further closure. By considering the so-called instantaneous dissipation rate $\varepsilon_0(\mathbf{x},t)$, proposed by Pope and Chen [24], Jayesh and Pope [25] formulated a model for the turbulence frequency ω, where $\omega = \varepsilon_0/k$ is the instantaneous turbulence frequency. By definition, ω is non-negative and different for each individual model particle. The model SDE they proposed reads

$$\mathrm{d}\omega^* = -(\omega^* - \langle\omega|X^*\rangle)\frac{\mathrm{d}t}{T_\omega(X^*)} - \langle\omega|X^*\rangle\omega^* S_\omega + \sqrt{\frac{2\sigma^2\langle\omega|X^*\rangle\omega^*}{T_\omega(X^*)}}\mathrm{d}W(t), \tag{27}$$

where $T_\omega(x)^{-1} = C_3\langle\omega|x\rangle$ is a timescale involving a model constant C_3. Another model constant is the normalized variance σ^2 of ω^*. In our case with $\partial\langle U_i\rangle/\partial x_j = 0$, the source term simplifies to $S_\omega = C_{\omega 2}$, where $C_{\omega 2}$ is a further model constant. In equilibrium, the PDF $f(\theta)$ of ω^*, modeled according to the SDE (27) (with $C_{\omega 2} = 0$), follows a gamma-distribution. Here, θ is the sample space variable of ω^*. Replacing the average dissipation rate $\varepsilon = \langle\varepsilon_0\rangle$ in Eq. (26) by $\langle\omega\rangle k$ leads to

$$\mathrm{d}u^* = -\left(\frac{1}{2} + \frac{3}{4}C_0\right)\langle\omega|X^*\rangle u^*\,\mathrm{d}t + \sqrt{C_0\langle\omega|X^*\rangle k(X^*)}\,\mathrm{d}W(t). \tag{28}$$

More details about the gamma-distribution model are given in [6].

Here, for numerical time integration of the model-particle transport Eq. (25), a forward Euler scheme is employed. To integrate the model-particle turbulence frequency Eq. (27) and the velocity evolution Eq. (28), the semi-implicit Milstein algorithm, outlined in [15] (Eqs. (10.4.16) and (10.4.17)), is applied. This algorithm has favorable stability properties and only in very rare cases, it leads to negative turbulence frequencies. Then $\omega^*(t + \mathrm{d}t)$ is reinitialized by a sample from a gamma-distribution with $\langle\omega|X^*(t)\rangle$ and normalized variance σ^2. At the domain inflow boundary, random number generators were used [26], providing Gaussian random numbers for the particle velocity and gamma-distributed random numbers for the turbulence frequency. To estimate particle statistics at the particle positions (e.g., $k(X^*)$ and $\langle\omega|X^*\rangle$), a particle-mesh method involving the linear kernel function (see Fig. 4)

$$K(r,h) = \begin{cases} 1 - \frac{|r|}{h} & \text{if } |r| \leqslant h, \\ 0 & \text{else,} \end{cases} \tag{29}$$

is used. On a one-dimensional grid with an equidistant spacing h, the average of a particle property Q^* can be estimated at the grid node $x^{(i)}$ as

$$\langle Q|x^{(i)}\rangle_{N,h} = \frac{\sum_{n=1}^{N} K(x^{(i)} - X^{*(n)}, h)Q^{*(n)}}{\sum_{n=1}^{N} K(x^{(i)} - X^{*(n)}, h)}, \tag{30}$$

where N is the number of model particles in the flow domain. Note that Q^* can be any function of particle properties, e.g., $(u^*)^2$. Finally, the average $\langle Q|X^*\rangle$ at the particle location X^* can be approximated by linear interpolation between grid nodes.

4.2. Validation of the PDF algorithm

Before we focus on the validation of the boundary condition implementations, it shall be shown that the one-dimensional PDF algorithm outlined above leads to a correct decay of k in DGT. Therefore, DGT was simulated and compared with the experimental case 'biplane, square-rod; $M = 2.54$ cm' listed in Table 3 of [22]. In this work, Comte-Bellot and Corrsin showed that the energies of the longitudinal and transversal fluctuating velocity components decay with identical parameters leading to the power law

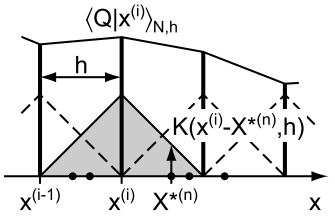

Fig. 4. Conceptual sketch of particle-mesh method with linear kernel function.

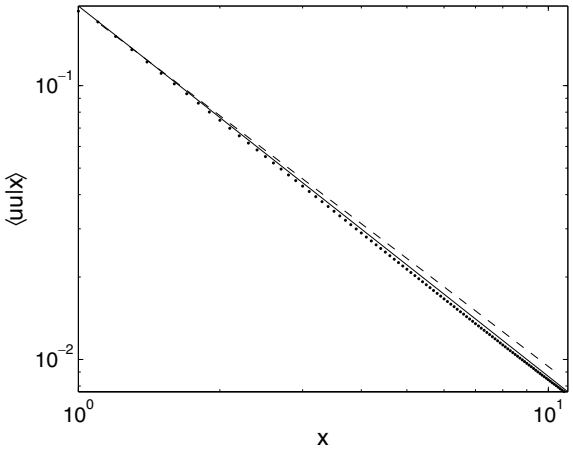

Fig. 5. Decay of $\langle uu|x\rangle$ as a function of the downstream position x in DGT. Solid line: power law with $n = 1.3$; dashed line: experiment of Comte-Bellot [22]; dots: numerical simulation.

$$\frac{k}{\langle U\rangle^2} = \frac{3}{2}\frac{1}{A}\left(\frac{x - x_o}{M}\right)^{-n} \tag{31}$$

for the turbulent kinetic energy. Here, A is a proportionality constant, x_o[3] a virtual origin on the downstream x-axis, M a grid lengthscale, and n the decay exponent. In the experiment by Comte-Bellot and Corrsin considered, these values are $\langle U\rangle = 10\ \mathrm{m/s}$, $x_o = 0.1016\ \mathrm{m}$ and n was varying between 1.28 and 1.29 but $n = 1.3$ is consistent with nearly all DGT data in the literature [6]. From Fig. 12 in [22] the inflow condition $u' = 0.442\ \mathrm{m/s}$ at $x = 1\ \mathrm{m}$ can be extracted. In a reference frame moving with $x = \langle U\rangle t$ we approximately have $\mathrm{d}k/\mathrm{d}t = -\varepsilon$ consistent with decaying homogeneous turbulence. Dividing this equation by k and combining it with Eq. (31) is giving

$$\langle \omega|x\rangle = n\frac{\langle U\rangle}{x - x_o}. \tag{32}$$

With this expression we obtain $\langle\omega|x\rangle = 14.47\ \mathrm{s}^{-1}$ as initial condition at $x = 1\ \mathrm{m}$. For the PDF simulation, 10,000 particles for a domain of 10 m in length were used and to estimate statistical moments an equidistant grid with 100 cells (101 nodes) was employed. Time integration was performed with a time-step size $\Delta t = 0.001\ \mathrm{s}$. For the model parameter C_0 in the SLM (28), the standard value $C_0 = 2.1$ was employed and for the ω-model, $C_3 = 1$, $\sigma^2 = 4$ and $C_{\omega 2} = 0.77$ [6] were used. With these choices, the time-averaged result depicted in Fig. 5 is obtained. As expected, this solution is in very good agreement with the decay exponent $n = 1.3$. Due to the relatively small ratio $u'/\langle U\rangle \approx 0.04$, the result is insensitive with respect to the boundary condition implementation.

4.3. Homogeneous test case

Aside from its non-convected counterpart, convected stationary homogeneous turbulence (CSHT) is the most simple turbulent flow. Since in the whole domain the turbulence intensity $u'/\langle U\rangle$ is the same as the one prescribed at the inflow boundary, it is a good configuration to test the boundary condition implementations. To obtain stationarity, $C_{\omega 2}$ was set to zero and the $\frac{1}{2}$ in Eq. (28) was omitted (p. 36 of [21]). In the simulations performed, aside from these modifications the same model parameters as in Section 4.2 were used. The turbulence intensity was varied between 50 and 0.125 with $u' = 0.5\ \mathrm{m/s}$ and $\langle U\rangle = 0.01, 0.05, 0.1, 0.25, 0.5, 1, 1.\bar{3}, 2, 4\ \mathrm{m/s}$. The mean turbulence frequency $\langle\omega\rangle$ was set to $2\ \mathrm{s}^{-1}$ and the time-step size to $\Delta t = 0.001\ \mathrm{s}$. The domain of 1 m in length was divided into 100 cells and 10,000 particles were used. Simula-

[3] Not to be confused with the initial position x_0 of moving walls.

tion results based on the convection dominated and moving-wall boundary condition implementations are presented in Figs. 6 and 7. Note that time averaging was employed in order to reduce the statistical error. Fig. 7 depicts the difference between the average velocity estimated from the particles and the one prescribed at the inflow boundary. First, the performance of the convection dominated implementations is discussed. As expected from the discussion of Eq. (15), the deviation of the average velocity at the inflow boundary is smallest for small and big turbulence intensities. At the outflow, however, it becomes larger for increasing turbulence intensities as discussed in Section 3.1. Of course, erroneous average velocities are connected with non-uniform particle position PDF's $f(x)$ as implied by Eq. (6) and shown in Fig. 6. Consequently, $f(x)$ is closest to uniform for small turbulence intensities $u'/\langle U\rangle$. The results based on the moving-wall implementation are independent of $u'/\langle U\rangle$, i.e., the particles are uniformly distributed within the domain and the expected particle velocity is equal to the specified one everywhere.

To verify the velocity PDF of the reflected particles (Eq. (21)), which was derived in Section 3.2.3, an additional simulation with moving-wall boundary conditions was performed. Here, the particle velocities at the inflow were not reassigned as described in connection with the mapping (24), but only reflected according

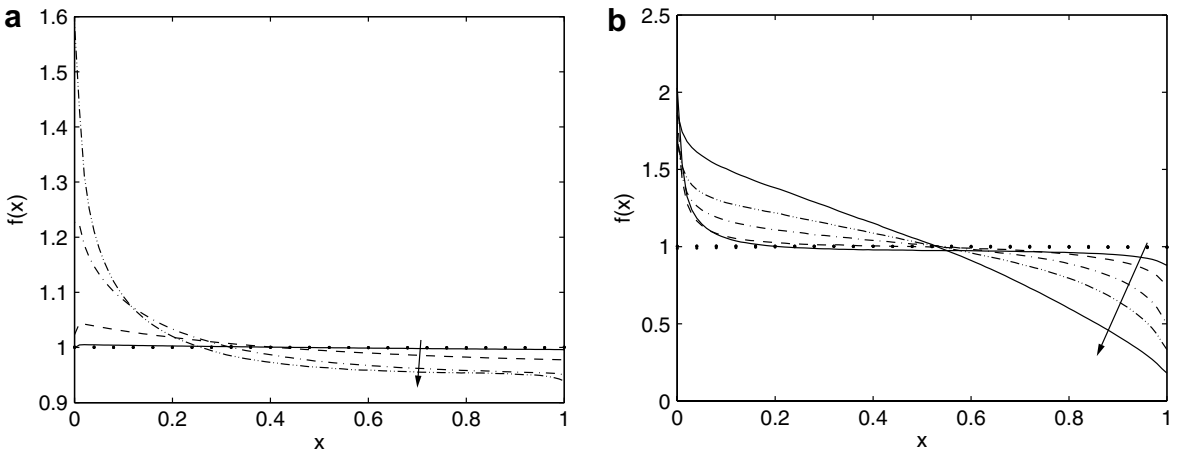

Fig. 6. Particle position PDF in CSHT simulations for different $u'/\langle U\rangle$ with $u' = 0.5$ m/s. Lines: convection dominated boundaries; dots: moving-wall boundaries. The arrows indicate decreasing $\langle U\rangle$: (a) $\langle U\rangle = 4, 2, 1.\bar{3}, 1$ m/s; (b) $\langle U\rangle = 0.5, 0.25, 0.1, 0.05, 0.01$ m/s.

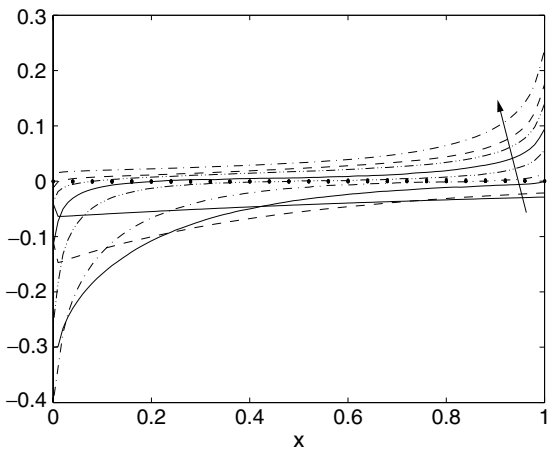

Fig. 7. Deviation between prescribed and computed average velocities in CSHT simulations for different $u'/\langle U\rangle$ (same values as in Fig. 6). Lines: convection dominated boundaries; dots: moving-wall boundaries. The arrow indicates decreasing $\langle U\rangle$.

to expression (14). (In the homogeneous case considered, reassigning and pure reflection lead to the same simulation results.) The reflected particle velocities at the inflow boundary were sampled over time and in Fig. 3 the resulting histogram is compared with the theoretical PDF (21). It can be seen that theory and numerical experiment are in exact agreement.

4.4. Inhomogeneous test case

The performance of the moving-wall boundary condition implementation was tested for inhomogeneous turbulence. Convected decaying turbulence (CDT) with high turbulence intensity at the inflow boundary was simulated, where the same parameters as in the CSHT case discussed in Section 4.3 with $\langle U \rangle = 1$ m/s were used. Other than in the CSHT case, the $\frac{1}{2}$ in the drift term of Eq. (28) was not omitted and $C_{\omega 2} = 0.77$ was used. The simulation results based on the different boundary condition implementations are summarized in Figs. 8 and 9. Like in the homogeneous case, the moving-wall boundaries provide far more consistent results. The particle position PDF (Fig. 8) is nearly uniform compared to the convection dominated approach, where the particles accumulate at the inflow. Consequently, the decay of $\langle uu|x \rangle$ is different (Fig. 9). The small error in

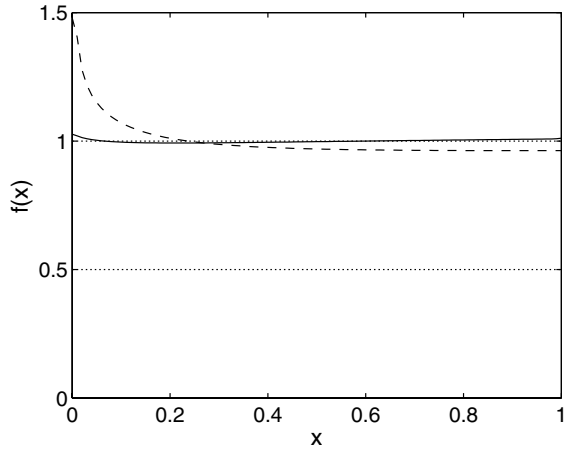

Fig. 8. Particle position PDF in CDT simulations for different boundary condition implementations. Solid line: moving wall; dashed line: convection dominated boundaries.

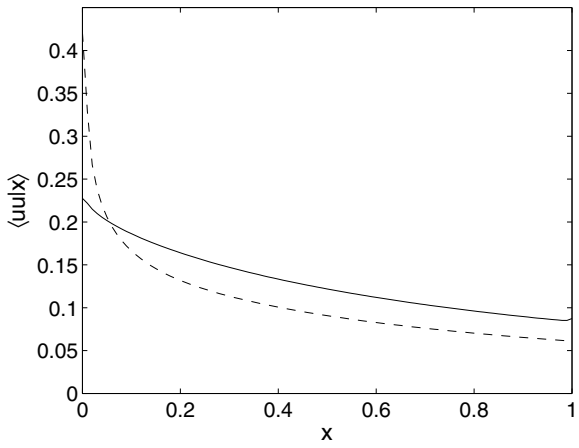

Fig. 9. Decay of $\langle uu|x \rangle$ as a function of the downstream position x in CDT for different boundary condition implementations. Solid line: moving wall; dashed line: convection dominated boundaries.

the particle position PDF near $x = 0$ of the simulation with moving wall might be further reduced, if the strong inhomogeneity of the velocity statistics near the boundary are taken into account for the velocity reassignment (Section 3.2.3).

5. Conclusions

Mass conservation leads to a consistency condition for the particle position PDF, which is relevant in both joint velocity–composition and joint composition PDF methods. In- and outflow boundary condition implementations should honor this condition. For joint velocity–composition PDF methods the convection dominated inflow implementation satisfies this condition for turbulence intensities approaching zero or infinity, whereas the outflow implementation is restricted to turbulence intensities approaching zero. In joint composition PDF methods, however, the convection dominated inflow boundary is consistent at all turbulence intensity levels, which is not the case for the outflow boundary. For particle buffer-layer boundary conditions, we have a tradeoff between layer thickness or time-step size, and consistency, which is governed by the local turbulence intensity. In this paper, in- and outflow boundary implementations, which are based on moving walls are outlined and successfully validated in different challenging numerical test cases. They cover both joint velocity–composition and joint composition PDF methods. At inflow boundaries of joint velocity–composition PDF methods, the marginal velocity PDF can be enforced by reassigning new velocities to the reflected particles. The presented implementations are simple and, most important, at all turbulence intensity levels honoring mass conservation. Moderate or high turbulence intensities at boundaries coincide typically with boundary layers that are present in simulations of, e.g., turbulent jets or mixing layers. Commonly applied mass conservation correction algorithms may hide errors originating from inconsistent implementations. Although only one-dimensional test cases are presented, the extension of the approach for two- or three-dimensional configurations is straightforward.

Acknowledgment

This work was supported by the Swiss National Science Foundation (SNF).

Appendix. Linearly varying wall velocity

Here, it is explained how to improve the moving-wall boundary condition implementation for $\langle U|x\rangle$ being variable in the vicinity of $x = x_b$. Therefore, we first approximate the mean velocity by a linear function in x. Consequently, the velocity of the moving wall becomes

$$u_w(x) = \langle U|x_b\rangle + \alpha(x - x_b), \quad \text{where } \alpha = \left.\frac{\partial\langle U|x\rangle}{\partial x}\right|_{x_b}. \tag{A.1}$$

As depicted in the sketch of Fig. A.1, the position of the moving wall is

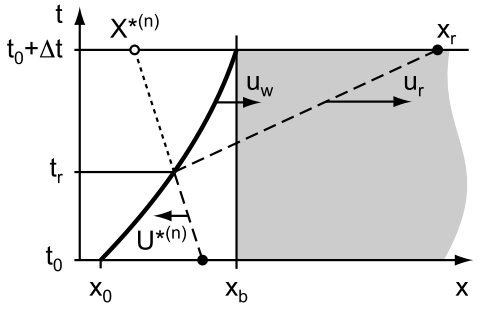

Fig. A.1. Particle reflection at moving-wall boundary with linearly varying wall velocity. The shaded area represents the flow domain and the thick line the moving wall.

$$x_w(t) = x_b + \alpha^{-1}\langle U|x_b\rangle\left[e^{\alpha(t-t_0-\Delta t)} - 1\right]. \tag{A.2}$$

The first three terms of the Taylor expansion of $x_w(t)$ around $t = t_0 + \Delta t$ read

$$x_w(t) = x_b + \langle U|x_b\rangle\left[(t - t_0 - \Delta t) + \frac{1}{2}\alpha(t - t_0 - \Delta t)^2\right]. \tag{A.3}$$

The particle trajectory at the moving wall prior to the reflection is $X^{*(n)} + U^{*(n)}(t - t_0 - \Delta t)$. At the intersection point, these two trajectories are equal and the corresponding intersection time is

$$t_r = t_0 + \Delta t - \frac{1}{\alpha\langle U|x_b\rangle}\left[\langle U|x_b\rangle - U^{*(n)} - \sqrt{(\langle U|x_b\rangle - U^{*(n)})^2 - 2\alpha\langle U|x_b\rangle(x_b - X^{*(n)})}\right]. \tag{A.4}$$

Finally, the position

$$\begin{aligned} x_r = {} & \langle U|x_b\rangle^{-2}\{\alpha^{-1}2(\langle U|x_b\rangle - 2U^{*(n)})(\langle U|x_b\rangle - U^{*(n)}) \\ & \times\left[\langle U|x_b\rangle - U^{*(n)} - \sqrt{(\langle U|x_b\rangle - U^{*(n)})^2 - 2\alpha\langle U|x_b\rangle(x_b - X^{*(n)})}\right] \\ & + 2\langle U|x_b\rangle\left[3U^{*(n)} + \sqrt{(\langle U|x_b\rangle - U^{*(n)})^2 - 2\alpha\langle U|x_b\rangle(x_b - X^{*(n)})}\right](x_b - X^{*(n)}) - \langle U|x_b\rangle^2(2x_b - 3X^{*(n)})\} \end{aligned} \tag{A.5}$$

and velocity

$$u_r = 2\langle U|x_b\rangle + 2\frac{U^{*(n)}}{\langle U|x_b\rangle}\left[U^{*(n)} + \sqrt{(\langle U|x_b\rangle - U^{*(n)})^2 - 2\alpha\langle U|x_b\rangle(x_b - X^{*(n)})}\right] - [3U^{*(n)} + 2\alpha(x_b - X^{*(n)})] \tag{A.6}$$

of the reflected particle can be computed.

References

[1] S.B. Pope, Advances in pdf methods for turbulent reactive flows, in: H.I. Andersson, P.A. Krogstad (Eds.), Proceedings of the 10th European Turbulence Conference, CIMNE, Trondheim, 2004, pp. 529–536.

[2] K. Liu, S.B. Pope, D.A. Caughey, Calculations of bluff-body stabilized flames using a joint probability density function model with detailed chemistry, Combustion and Flame 141 (1–2) (2005) 89–117.

[3] D.W. Meyer, P. Jenny, A mixing model for turbulent flows based on parameterized scalar profiles, Physics of Fluids 18 (3) (2006).

[4] S.B. Pope, Pdf methods for turbulent reactive flows, Progress in Energy and Combustion Science 11 (2) (1985) 119–192.

[5] R.O. Fox, Computational Models for Turbulent Reacting Flows, Cambridge University Press, Cambridge, 2003.

[6] S.B. Pope, Turbulent Flows, Cambridge University Press, Cambridge, 2000.

[7] S.B. Pope, Consistency conditions for random-walk models of turbulent dispersion, Physics of Fluids 30 (8) (1987) 2374–2379.

[8] R.R. Cao, S.B. Pope, A.R. Masri, Turbulent lifted flames in a vitiated coflow investigated using joint pdf calculations, Combustion and Flame 142 (4) (2005) 438–453.

[9] M. Muradoglu, P. Jenny, S.B. Pope, D.A. Caughey, A consistent hybrid finite-volume/particle method for the pdf equations of turbulent reactive flows, Journal of Computational Physics 154 (2) (1999) 342–371.

[10] M.S. Anand, A.T. Hsu, S.B. Pope, Calculations of swirl combustors using joint velocity scalar probability density function method, AIAA Journal 35 (7) (1997) 1143–1150.

[11] M.S. Anand, S.B. Pope, H.C. Mongia, A pdf method for turbulent recirculating flows, in: R. Borghi (Ed.), Proceedings of the USA France Joint Workshop on Turbulent Reactive Flows, Springer, 1989, pp. 673–692.

[12] R.P. Lindstedt, S.A. Louloudi, E.M. Vaos, Joint scalar probability density function modeling of pollutant formation in piloted turbulent jet diffusion flames with comprehensive chemistry, Proceedings of the Combustion Institute 28 (2000) 149–156.

[13] T. Hulek, R.P. Lindstedt, Joint scalar-velocity pdf modelling of finite rate chemistry in a scalar mixing layer, Combustion Science and Technology 136 (1–6) (1998) 303–331.

[14] W.C. Welton, S.B. Pope, Pdf model calculations of compressible turbulent flows using smoothed particle hydrodynamics, Journal of Computational Physics 134 (1) (1997) 150–168.

[15] C.W. Gardiner, Handbook of Stochastic Methods for Physics, Chemistry and the Natural Sciences, third ed., Springer, Berlin, 2004.

[16] L. Valino, J. Hierro, Boundary conditions for probability density function transport equations in fluid mechanics, Physical Review E 67 (4) (2003).

[17] B. Rembold, P. Jenny, A multiblock joint pdf finite-volume hybrid algorithm for the computation of turbulent flows in complex geometries, Journal of Computational Physics 220 (1) (2006) 59.
[18] Y.Z. Zhang, D.C. Haworth, A general mass consistency algorithm for hybrid particle/finite-volume pdf methods, Journal of Computational Physics 194 (1) (2004) 156–193.
[19] M. Muradoglu, S.B. Pope, D.A. Caughey, The hybrid method for the pdf equations of turbulent reactive flows: consistency conditions and correction algorithms, Journal of Computational Physics 172 (2) (2001) 841–878.
[20] T. Werder, J.H. Walther, P. Koumoutsakos, Hybrid atomistic-continuum method for the simulation of dense fluid flows, Journal of Computational Physics 205 (1) (2005) 373–390.
[21] S.B. Pope, Lagrangian pdf methods for turbulent flows, Annual Review of Fluid Mechanics 26 (1994) 23–63.
[22] G. Comte-Bellot, S. Corrsin, The use of a contraction to improve isotropy of grid-generated turbulence, Journal of Fluid Mechanics 25 (1966) 657–682.
[23] M.S. Anand, S.B. Pope, Diffusion behind a line source in grid turbulence, in: L.J.S. Bradbury (Ed.), Proceedings of the Fourth International Symposium on Turbulent Shear Flows, Springer-Verlag, Karlsruhe, 1983, pp. 46–61.
[24] S.B. Pope, Y.L. Chen, The velocity-dissipation probability density-function model for turbulent flows, Physics of Fluids A-Fluid Dynamics 2 (8) (1990) 1437–1449.
[25] Jayesh, S.B. Pope, Stochastic model for turbulent frequency, Tech. Rep. FDA 95-05, Cornell University, 1995.
[26] W.H. Press, Numerical Recipes in Fortran 77 the Art of Scientific Computing, second ed., Cambridge University Press, Cambridge, 2001.